Peering into buried interfaces with X-rays and electrons to unveil $MgCO_3$ formation during CO_2 capture in molten salt-promoted MgO

Alexander H. Bork[a,1], Margarita Rekhtina[a,1], Elena Willinger[a,2], Pedro Castro-Fernández[a], Jakub Drnec[b], Paula M. Abdala[a,2], and Christoph R. Müller[a,2]

[a]Laboratory of Energy Science and Engineering, Department of Mechanical and Process Engineering, Eidgenössische Technische Hochschule (ETH) Zürich, 8092 Zürich, Switzerland; and [b]European Synchrotron Radiation Facility, 38000 Grenoble, France

Edited by Alexis T. Bell, University of California, Berkeley, CA, and approved May 21, 2021 (received for review February 28, 2021)

The addition of molten alkali metal salts drastically accelerates the kinetics of CO_2 capture by MgO through the formation of $MgCO_3$. However, the growth mechanism, the nature of $MgCO_3$ formation, and the exact role of the molten alkali metal salts on the CO_2 capture process remain elusive, holding back the development of more-effective MgO-based CO_2 sorbents. Here, we unveil the growth mechanism of $MgCO_3$ under practically relevant conditions using a well-defined, yet representative, model system that is a MgO(100) single crystal coated with $NaNO_3$. The model system is interrogated by in situ X-ray reflectometry coupled with grazing incidence X-ray diffraction, scanning electron microscopy, and high-resolution transmission electron microscopy. When bare MgO(100) is exposed to a flow of CO_2, a noncrystalline surface carbonate layer of *ca.* 7-Å thickness forms. In contrast, when MgO(100) is coated with $NaNO_3$, $MgCO_3$ crystals nucleate and grow. These crystals have a preferential orientation with respect to the MgO(100) substrate, and form at the interface between MgO(100) and the molten $NaNO_3$. $MgCO_3$ grows epitaxially with respect to MgO(100), and the lattice mismatch between $MgCO_3$ and MgO is relaxed through lattice misfit dislocations. Pyramid-shaped pits on the surface of MgO, in proximity to and below the $MgCO_3$ crystals, point to the etching of surface MgO, providing dissolved $[Mg^{2+}\ldots O^{2-}]$ ionic pairs for $MgCO_3$ growth. Our studies highlight the importance of combining X-rays and electron microscopy techniques to provide atomic to micrometer scale insight into the changes occurring at complex interfaces under reactive conditions.

CO_2 | carbonate | interfaces | X-rays | microscopy

Global concerns about the rising level of greenhouse gas emissions and the associated climate change require the development of efficient processes to remove CO_2 selectively from large point sources or directly from the atmosphere. Such processes are termed carbon dioxide capture and storage (CCS) (1) and can be implemented on the industrial scale in different configurations such as precombustion, postcombustion, or oxy-combustion CCS (2, 3). A large variety of both liquid and solid sorbent materials have been explored for CCS, with solid CO_2 sorbents being particularly interesting owing to their ability to capture large quantities of CO_2 from point sources with, compared to amines, favorable efficiency and cost penalty estimates (4). Yet, the development of inexpensive solid sorbents that capture CO_2 with fast rates, possess a high CO_2 capacity, and operate with high stability over many CO_2 capture and regeneration cycles remains a key challenge. To advance the current state of sorbent design in a rational fashion, an improvement of our current understanding of the interplay between a sorbent's structural features and its CO_2 capture characteristics is required.

Magnesium oxide (MgO) is an attractive solid CO_2 sorbent, in particular for precombustion CCS applications, that stands out owing to its high theoretical CO_2 uptake of 1.09 $g_{CO2}{\cdot}g_{MgO}^{-1}$ (24.8 $mmol_{CO2}{\cdot}g_{MgO}^{-1}$) and relatively low temperature for regeneration, as compared to other solid sorbents (e.g., CaO, Li_4SiO_4, and Li_2ZrO_3). Despite its high theoretical CO_2 capacity, bare MgO displays very sluggish carbonation kinetics, yielding an experimental CO_2 uptake of only 0.02 $g_{CO2}{\cdot}g_{MgO}^{-1}$ after 1 h of exposure to CO_2 (5, 6). The low practically obtained CO_2 uptake compared to the high theoretical value has been attributed to the high lattice enthalpy of MgO reducing the kinetics of its reaction with CO_2 appreciably and to the formation of a monodentate carbonate layer on the surface of MgO, which acts as a CO_2-impermeable barrier hampering the further conversion of unreacted MgO (7–9). Encouragingly, the slow uptake of MgO can be accelerated appreciably through an engineering solution, that is, the addition of alkali metal salts (AMS; e.g., $NaNO_3$, KNO_3, $LiNO_3$, and their eutectic mixtures) which are molten at operating conditions (10–14). By optimizing the loading of AMS (*ca.* 20 wt. % AMS), the CO_2 uptake of MgO can be increased by a factor of 15 (0.31 $g_{CO2}{\cdot}g_{sorbent}^{-1}$) compared to unpromoted MgO at identical carbonation durations (13). The kinetics and stability of AMS-promoted MgO can be improved even further when adding alkali earth carbonates such as $SrCO_3$ or $CaCO_3$, which have been hypothesized to act as nucleation seeds or to lead to the formation of double carbonate phases that form with faster kinetics. For such systems, CO_2 uptakes of up to 0.65 $g_{CO2}{\cdot}g_{sorbent}^{-1}$ after 50 carbonation and calcination cycles have been reported (15–17).

Significance

The grand challenge of reducing CO_2 emissions requires the development of cost-effective CO_2 sorbents. Based on the theoretically obtainable weight-normalized CO_2 uptake, MgO-based materials promoted with molten salts are attractive sorbents when compared to amines or metal organic frameworks. However, there is very little understanding of the processes that occur at the atomic-to-micro scale during CO_2 capture conditions, hampering the advancement of such sorbents. Combining X-ray and electron-based characterization techniques, we observe that $MgCO_3$ crystals form via nucleation and growth at the interface between MgO and the molten salt and are oriented with respect to the MgO(100) surface. Hence, more-effective MgO-based sorbents will require maximizing the interfacial area and the number of nucleation sites at the interface.

Author contributions: A.H.B., M.R., E.W., P.M.A., and C.R.M. designed research; A.H.B., M.R., E.W., P.C.-F., J.D., and P.M.A. performed research; A.H.B., M.R., E.W., P.C.-F., J.D., and P.M.A. analyzed data; and A.H.B., M.R., E.W., P.M.A., and C.R.M. wrote the paper.

The authors declare no competing interest.

This article is a PNAS Direct Submission.

[1]A.H.B. and M.R. contributed equally to this work.

[2]To whom correspondence may be addressed. Email: elenawi@ethz.ch, abdalap@ethz.ch, or muelchri@ethz.ch.

This article contains supporting information online at https://www.pnas.org/lookup/suppl/doi:10.1073/pnas.2103971118/-/DCSupplemental.

Published June 17, 2021.

Owing to the impressive effect of molten AMS on the CO_2 uptake of bare MgO, the elucidation of the underlying promoting mechanism(s) has been the aim of a series of studies that have led to the postulation of a number of working hypotheses (12, 13, 16, 18–22). For example, combining thermogravimetric analysis (TGA), Fourier transform infrared spectroscopy (FTIR), and powder X-ray diffraction (XRD), it has been proposed that the addition of AMS promotes the CO_2 uptake of MgO through the following two effects. Firstly, it has been argued that AMS prevent the formation of a CO_2-impermeable monodentate carbonate layer on the surface of MgO, and they dissolve CO_2 that reacts with oxide ions (O^{2-}) in the nitrate (23), leading to the formation of reactive carbonate ions (CO_3^{2-}) that subsequently react with Mg^{2+} to form $MgCO_3$ (13). A second hypothesis, based on TGA and density functional theory (DFT) calculations, has argued that the promoting role of the AMS is mainly due to the molten salt's ability to lower the energy barrier associated with the high lattice enthalpy of MgO by dissolving the solid metal oxide (12, 18). The dissolution of MgO in the molten promoter yields solvated [$Mg^{2+}\ldots O^{2-}$] ionic pairs that have weaker bonds compared to the strong ionic bonds in bulk MgO (12). The DFT calculations showed that the rate-controlling step for the reaction between CO_2 and MgO is the activation of the MgO ionic bond; the energy barrier to form [$Mg^{2+}\ldots O^{2-}$] ionic pairs in the molten $NaNO_3$ is 5.33 eV, compared to 7.07 eV without $NaNO_3$ (12). The dissolved ionic pair reacts with CO_2 that is adsorbed on the MgO surface, that is, at the triple phase boundary (TPB) between MgO, CO_2, and the molten phases, to form [$Mg^{2+}\ldots CO_3^{2-}$] ionic pairs. Upon reaching saturation, the [$Mg^{2+}\ldots CO_3^{2-}$] ionic pairs precipitate as a crystalline $MgCO_3$ phase. It is further argued that the carbonate may precipitate away from the original dissolution site so as to not prohibit further reaction. Following this argument, the reaction would, in theory, continue until MgO is completely converted. However, in practice, MgO conversion stops at ~70%, which has been argued to arise from a reducing TPB length. A recent in situ total scattering study points to a more multifaceted role of the AMS promoter in the MgO–CO_2 system, as the AMS do not affect only the nucleation of $MgCO_3$ but also the microstructure and growth of the $MgCO_3$ formed (20).

Turning to the kinetics of CO_2 absorption, TGA-based studies of $NaNO_3$-promoted MgO powders have shown that the formation of $MgCO_3$ is characterized by a nucleation and growth process (16). The characteristic sigmoidal kinetic curve of MgO conversion suggests that the carbonate formation is "autocatalytic"; that is, once a stable nucleation seed is formed, the growth rate is accelerated. This interpretation was corroborated by experimental evidence that showed that the induction period, that is, the time required for the first stable nuclei to form, can be shortened by the inclusion of "inert" $SrCO_3$ seeds, which act as nucleation sites for $MgCO_3$ (16). Although there is a general agreement on the nucleation- and growth-based mechanism for the formation of $MgCO_3$, there are competing hypotheses on the nature of magnesium carbonate formation, that is, where it forms (at the interface AMS/MgO, at the TPB, or inside the AMS), its growth habit, and its morphology. According to an in situ TEM study of MgO nanoparticles that were physically mixed with a eutectic mixture of AMS, $MgCO_3$ nucleates favorably at the TPB (24, 25). Nonetheless, a different study suggests that the TPB is not a necessary condition for the absorption to take place, as carbonates ($MgCO_3$) were detected on the surface of a MgO(100) single crystal that was covered completely by $NaNO_3$ and treated under CO_2 (330 °C), as revealed by ex situ FTIR after the removal of $NaNO_3$ (16). Jo et al. (16) proposed that $MgCO_3$ is formed inside the molten promoter through nucleation and growth steps.

Hence, despite extensive efforts, the mechanisms behind the promoting role of AMS on MgO-based CO_2 sorbents have not been unveiled yet. Atomic-level insight into the promoting effect of AMS would allow unlocking of the full potential of MgO-based CO_2 sorbents and design materials that approach (repeatedly) full conversion over a large number of CO_2 capture and regeneration cycles. To obtain such atomic-level insight, well-defined model systems and interrogation of them with detailed (in situ) characterization techniques are required. In this study, we utilize a single-crystal MgO(100) surface [the most stable and abundant MgO facet (21, 26, 27)] coated with $NaNO_3$ and probe, in detail, its structural dynamics under CO_2 capture conditions. Synchrotron-based, in situ X-ray reflectometry (XRR) and grazing incidence XRD (GIXRD) unravel the changes occurring at the surface of MgO under CO_2 capture condition (allowing study of the buried interface between the $NaNO_3$ promoter and MgO). We complemented the in situ X-ray–based characterizations by (ex situ) scanning electron microscopy (SEM) to characterize, in detail, the morphology of the $MgCO_3$ product formed (after carbonation and after removing the $NaNO_3$ promoter). Our studies evidence the formation of a noncrystalline carbonate layer on bare MgO(100) under CO_2 capture conditions. In contrast, MgO(100) coated with $NaNO_3$ exhibited an island-type growth of $MgCO_3$, as opposed to a homogeneous surface layer growth. $MgCO_3$ grows in a highly oriented fashion with a sectored-plate habit growth at the interface between $NaNO_3$/MgO(100), following a nucleation and growth mechanism. High-resolution TEM (HRTEM) provided atomic-level insight into the $MgCO_3$/MgO interface, evidencing an epitaxial arrangement between $MgCO_3$ and MgO whereby the lattice mismatch between $MgCO_3$ and MgO is relaxed through lattice misfit dislocations.

Results and Discussion

Changes at the Surface of MgO under CO_2 Capture Conditions Probed by In Situ XRR-GIXRD. To gain atomic-scale insight into the morphological and structural changes at the surface of MgO(100) and at the interface between MgO(100) and molten $NaNO_3$ under CO_2 capture conditions, we employed in situ high-energy (70 KeV) XRR and GIXRD. XRR probes the morphology of surfaces and interfaces at the atomic scale, even in the absence of long-range order, providing information about the average electronic density profile (scattering length density) as a function of probing depth (28). GIXRD provides complementary information on the crystalline phases close to the surface of the material. The consecutive acquisition of both in situ XRR and GIXRD data was carried out using a quartz dome cell connected to a gas control system. A schematic of the setup is shown in Fig. 1*A* and *SI Appendix*, Fig. S2. The grazing incident geometry and the high photon flux of the synchrotron radiation source enhanced the surface sensitivity, while the high photon energy was beneficial to penetrate the sample environment. The setup allowed us to acquire consecutive XRR and GIXRD data under relevant CO_2 capture conditions on bare MgO(100) and $NaNO_3$-coated MgO(100) (Fig. 1*A* and *SI Appendix*, Figs. S2 and S3). First, the samples were pretreated in situ in He at 450 °C for *ca.* 15 min to remove adsorbed water, hydroxides, and carbonates adsorbed onto the surface (29–31) and were subsequently cooled down to 330 °C in He. The collected XRR data on bare MgO(100) and $NaNO_3$-coated MgO(100) at 330 °C under He flow are referred to as $MgO(100)_{-He}$ and $NaNO_3$-$MgO(100)_{-He}$, respectively. The He pretreatment was followed by exposing the samples to a CO_2 flow (10 mL·min^{-1}) for *ca.* 90 min ($MgO(100)_{-CO2}$ and $NaNO_3$-MgO-$(100)_{-CO2}$, respectively). GIXRD patterns were collected consecutively after the respective XRR measurements (*SI Appendix*, Fig. S3).

The experimental and fitted XRR curves, plotting the intensity of the reflected X-rays as a function of the scattering vector Q_z normal to the surface (where $Q_z = 4\pi/\lambda \cdot \sin\alpha$, and α is the incident angle), are presented in Fig. 1*B*. A typical XRR curve includes the following features: 1) a total reflection region below the critical angle which is determined by the difference in the electron densities of the gas phase and the surface of MgO and 2) a reflectivity region above the critical angle, described by a combination of a

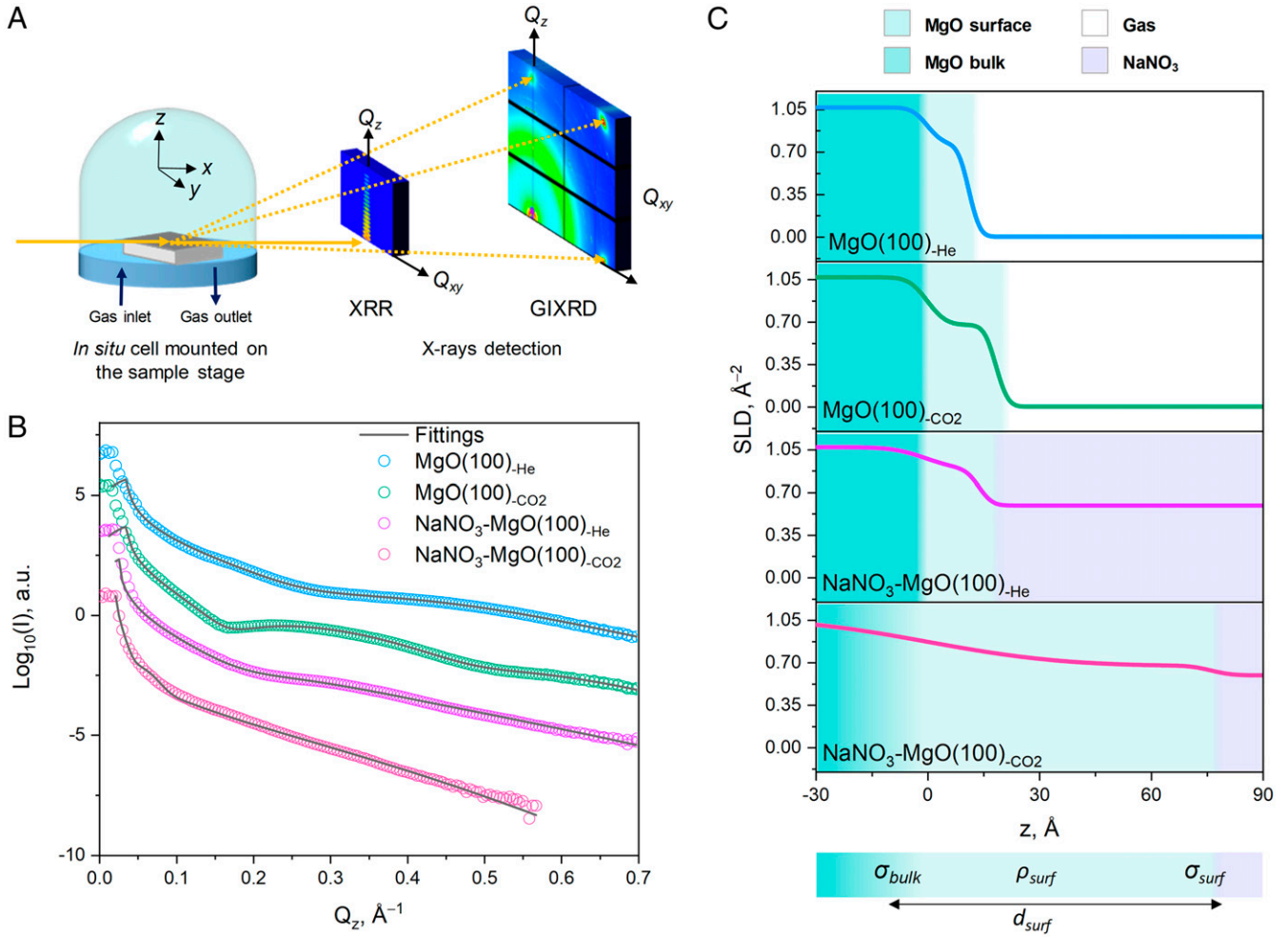

Fig. 1. (*A*) Schematic illustration of the in situ XRR-GIXRD setup. (*B*) Experimental (open circles) and fitted (gray lines) XRR curves for $MgO(100)_{-He}$, $MgO(100)_{-CO2}$, $NaNO_3$-$MgO(100)_{-He}$, and $NaNO_3$-$MgO(100)_{CO2}$. The curves are offset vertically by two orders of magnitude for clarity. The XRR data are modeled via a layered structure model consisting of following components: 1) bulk MgO substrate, 2) a surface layer with a lower electronic density (slab due to surface hydroxide and carbonate species and surface imperfections) and 3) slab of a molten $NaNO_3$ phase for the $NaNO_3$-MgO(100) system. A misfit in the region below the critical angle is ascribed to the finite length and nonzero curvature of the crystal (65). (*C*) The scattering length density (SLD), i.e., electron density profiles obtained from the modeling; the colors represent the "bulk MgO" substrate, the surface layer, the gas phase, and the $NaNO_3$ coat, with their corresponding thickness, *d*, density, ρ, and roughness, σ. The fitted parameters were σ_{bulk}, σ_{surf}, d_{surf}, and ρ_{surf}, where the subscripts "*bulk*" and "*surf*" refer to the bulk MgO substrate and the surface layer, respectively. The fixed parameters are $\rho_{bulk\text{-}MgO}$ = 3.57 g/cm^3, ρ_{NaNO3} = 1.9 g/cm^3, $d_{bulk} = \infty$, $d_{Gas} = \infty$, and $d_{NaNO3} = \infty$ (*SI Appendix*, Table S1).

rapid decay in the reflected intensity (Fresnel reflectivity curve) and the oscillation (Kiessig) fringes (32, 33). The Fresnel curve and the Kiessig fringes are related to the morphology and electronic density of the surface layer(s) (*SI Appendix*, Fig. S4). Modeling of the XRR data allows determination of the electronic density profiles normal to the surface (Fig. 1*C*), yielding, in turn, the average thickness, density, and roughness of the layer(s) close to the surface of a material. The fitting results are provided in *SI Appendix*, Table S1 and the fitting parameters are illustrated in the schematic in Fig. 1*C* and *SI Appendix*, Fig. S6.

The experimental XRR curve of $MgO(100)_{-untreated}$ (*SI Appendix*, Fig. S7) exhibits Kiessig fringes in the range of 0.1 Å^{-1} to 0.4 Å^{-1}. These fringes can be attributed to both the presence of imperfect terminations at both the surface and subsurface of the crystal (34) and adsorbed species (such as water, hydroxyl, and carbonates due to exposure of the crystal to ambient conditions prior to the experiment; *SI Appendix*, Fig. S5) (21, 35). The presence of a defective surface is in line with previous studies (using ultraviolet diffuse reflectance and scanning tunneling microscopy) that have described the MgO(100) surface as composed of terraces of different heights, separated by defects such as steps and kinks (36–40). $MgO(100)_{-He}$ exhibits a subtle Kiessig fringe at *ca.* 0.3 Å^{-1} to 0.7 Å^{-1} (Fig. 1*B*). Comparing $MgO(100)_{-He}$ to the untreated sample $MgO(100)_{-untreated}$, we observed that pretreatment leads to a decrease in the fringe periodicity and its amplitude that translates to a decrease of the thickness of the surface layer as can be seen from the electronic density profile (Fig. 1*B* and *SI Appendix*, Fig. S7). This indicates that the adsorbed surface groups have been (partially) removed after the thermal treatment in He. However, the complete removal of all of the surface species would require higher temperatures; thus residual hydroxyl and carbonates species remain on $MgO(100)_{-He}$ (21). This is in line with in situ diffuse reflectance infrared Fourier transform spectroscopy (DRIFTS) results, showing that carbonates and hydroxyl groups (adsorbed onto the surface of untreated MgO) are partially removed after a treatment in an inert atmosphere at 450 °C (*SI Appendix*, Fig. S5). Thus, the surface of $MgO(100)_{-He}$ can be considered as an imperfect MgO surface containing also residual adsorbed hydroxyl and carbonates species. Accordingly, to fit the XRR data, we have used a model composed of 1) a semiinfinite substrate representing the bulk MgO and 2) a slab to model the

surface layer, referred to as "bulk MgO" and "surface layer," respectively (Fig. 1*B* and *SI Appendix*, Table S1). The thickness of the surface layer in $MgO(100)_{-He}$ was found to be *ca.* d_{surf} = 11 Å. The roughness of the surface layer (σ_{surf}), defined as the root-mean-square elevation of the surface contour (41), was determined to be 2.4 Å, while the roughness of the interface between the bulk and surface MgO layers equals 3.3 Å. The density of the surface layer in $MgO(100)_{-He}$ was determined to be 2.6 g/cm^3, that is, 75% of the bulk density of MgO. Overall, the decrease in thickness of the surface layer, d_{surf}, and decrease in interface roughness, σ_{bulk}, after 15 min of treatment in He at 450 °C is very likely due to the decomposition of surface species and a temperature-induced smoothening of the surface. Smoothening of a MgO(100) surface has been observed previously after thermal treatment using atomic force microscopy (35).

A noticeable change in the XRR curve can be observed for $MgO(100)_{-CO2}$ as compared to $MgO(100)_{-He}$. The XRR of $MgO(100)_{-CO2}$ shows a pronounced well-defined fringe between *ca.* 0.2 and 0.5 Å^{-1}, indicating a thicker surface layer that is ascribed to the formation of carbonates on the surface. The calculated electronic density profile (Fig. 1*C*) shows an increase in the thickness of the surface layer by *ca.* 7 Å (d_{surf} = 18 Å, σ_{surf} = 2.5 Å, and σ_{bulk} = 4.0 Å $MgO(100)_{-CO2}$; *SI Appendix*, Table S1) and a decrease in the density of the surface layer of $MgO(100)_{-CO2}$ to 2.3 g/cm^3 when compared to $MgO(100)_{-He}$. Previous combined DRIFTS and DFT studies have shown that CO_2 is adsorbed preferentially as a monodentate carbonate species at surface defects of MgO(100), such as undercoordinated $O^{2-}{}_{4C}$ steps and $O^{2-}{}_{3C}$ kinks (21, 30, 42). In line with these studies, in situ DRIFTS analysis on a MgO powder (*SI Appendix*, Fig. S5) confirms that a partially cleaned MgO surface (by thermal treatment in an inert atmosphere) shows the formation of carbonates and bicarbonates (the latter formed through the reaction of CO_2 with surface hydroxyls) after exposure to a CO_2 flow at 330 °C, indicating that the increase in the thickness of the surface layer can be attributed to adsorbed carbonates. The XRR results are consistent with the observation that the GIXRD pattern of $MgO(100)_{-CO2}$ (*SI Appendix*, Figs. S8 and S10) shows no crystalline $MgCO_3$, indicating that the formation of carbonates on bare MgO(100) is largely limited to the surface, in line with previous studies (18, 21).

Turning to the $NaNO_3$-promoted material, to model the XRR data of $NaNO_3$-$MgO(100)_{-He}$, we use an additional infinitely thick slab to account for the molten $NaNO_3$, yielding a model that consists now of 1) "bulk MgO", 2) "surface layer," and 3) "molten $NaNO_3$" (Fig. 1*C*). The model yields a thickness of 14 Å for the surface layer at the $NaNO_3$/MgO interface, with a density of 2.9 g/cm^3 (*ca.* 80% of the bulk density of MgO). We observe that the thickness and average electronic density of the surface layer of $NaNO_3$-$MgO(100)_{-He}$ are comparable to $MgO(100)_{-He}$ within the experimental error. Here, the modeled thicknesses are 11 and 14 Å and the densities are 2.6 and 2.9 g/cm^3, for $MgO(100)_{-He}$ and $NaNO_3$-$MgO(100)_{-He}$, respectively (*SI Appendix*, Table S1). Based on these observations, we assume that, under identical (inert) pretreatment conditions, the presence of $NaNO_3$ does not lead to significant differences in the amount of remaining hydroxide and/or carbonate species on the respective surfaces. Interestingly, the roughness of the "bulk MgO," σ_{bulk}, increases to *ca.* 7.3 Å in comparison to 3.3 Å for $MgO(100)_{-He}$. We interpret this roughening of the MgO(100) surface by the dissolution of surface MgO [Mg^{2+} and O^{2-}] into the molten $NaNO_3$ (12, 18). Thus, our XRR measurements provide in situ evidence of the modification of the MgO(100) surface (partial dissolution of [Mg^{2+}...O^{2-}] ionic pairs) by molten salts.

XRR data of the $NaNO_3$-promoted sample, after its exposure to CO_2 ($NaNO_3$-$MgO(100)_{-CO2}$), show a more rapid intensity decrease with Q_z when compared to $NaNO_3$-$MgO(100)_{-He}$. In addition, we cannot observe any Kiessig fringes. These results indicate that a significant roughening of the surface must have occurred (Fig. 1*C*). Fitting with the three-layer model yielded a significant increase in σ_{bulk} (the roughness of the interface between the bulk MgO and surface layer) to 29 Å (*SI Appendix*, Table S1) which is approximately 4 and 7 times higher than that in $NaNO_3$-$MgO(100)_{-He}$ and $MgO(100)_{-CO2}$, respectively. It should be noticed that the "surface layer" in $NaNO_3$-$MgO(100)_{-CO2}$ is associated with the formation of $MgCO_3$. Hence, changes in σ_{bulk} represent an average roughness of the $MgCO_3$/MgO interface, while the thickness of the surface layer reflects the average thickness of the $MgCO_3$ product. This observation has two important implications. First, the $MgCO_3$ product is not formed as a homogenous, flat layer on the surface of MgO(100), in agreement with electron microscopy studies (*vide infra*). Second, the (structural) transformation of the MgO surface layer (i.e., the MgO/$NaNO_3$ interface), as quantified by its total roughness, is at least 4 times more pronounced when the $NaNO_3$-promoted sample is exposed to CO_2 compared to the surface restructuring arising purely due to the presence of $NaNO_3$. It should be noticed that XRR provides averaged information of the changes occurring at the MgO/$NaNO_3$ interface; the exact morphology (size and shape) of the $MgCO_3$ product will be assessed by electron microscopy (*vide infra*) that provides local information of the surface morphology.

To probe, in more detail, the formation of crystalline phases at the surface of the promoted material, we employ in situ GIXRD. In GIXRD data, a single crystal appears as dots, while a polycrystalline material with randomly oriented crystallites would reveal itself in the form of Debye–Scherrer rings with a homogeneous distribution of intensities along the azimuthal angle relative to the incident X-ray beam angle, φ. The crystal orientation is characterized by the distribution of intensities along φ (43, 44). The two-dimensional (2D) pattern of $NaNO_3$-$MgO(100)_{-He}$ (*SI Appendix*, Fig. S9) shows single crystalline Bragg reflections (bright spots) due to the (200), (020), and (220) planes of MgO, indicative of the single crystal nature of the MgO(100) substrate (space group *Fm–3m*; Inorganic Crystal Structure Database (ICSD): 9863); we could not observe rings, due to polycrystalline MgO. Since $NaNO_3$ is molten under the experimental, in situ conditions employed, no Bragg reflections due to the $NaNO_3$ phase are present in the GIXRD patterns, yet an amorphous halo due to diffuse scattering of molten $NaNO_3$ is observed at *ca.* 1.5 Å^{-1}. The corresponding GIXRD 2D pattern of $NaNO_3$-$MgO(100)_{-CO2}$ (Fig. 2*A*) reveals reflections due to crystalline $MgCO_3$ (space group *R–3c*; ICSD: 40117). The $MgCO_3$ reflections appear as spotty diffraction rings, revealing a preferred distribution of intensities at certain values of φ, highlighting that the $MgCO_3$ product consists of crystals with a marked preferred orientation (more insight into the orientation and size of the $MgCO_3$ crystals is gained by electron microscopy, *vide infra*). To analyze the distribution of the orientations of the crystallites formed, we plot the intensities of the $MgCO_3$(104) and $MgCO_3$(006) reflections as a function of φ (Fig. 2*C*). This analysis shows that a large proportion of the $MgCO_3$(104) and $MgCO_3$(006) reflections are preferably oriented at *ca.* φ = 10°, 45°, and 90°. Thus, these in situ GIXRD experiments reveal the formation of well-defined crystalline domains with a marked orientation along the [200], [220], and [020] directions of the MgO(100) substrate during product growth (Fig. 2*A*). The growth of $MgCO_3$ was analyzed with atom-scale resolution by HRTEM and will be discussed in more detail further below.

To probe the vertical location of the $MgCO_3$ product with respect to the $NaNO_3$/MgO interface, we collected GIXRD while varying the position of the sample in the *z* direction with respect to the incident beam (Fig. 1*A*). This scan was performed between *ca.* 30 μm above and *ca.* 10 μm below the $NaNO_3$/MgO interface, with a step size of 2 μm, providing information on the spatial distribution of the crystalline phases (*SI Appendix*, Fig. S11). *SI Appendix*, Fig. S12 plots the integrated intensities of the $MgCO_3$(104) and MgO(220) reflections as a function of the *z* position with regard to the $NaNO_3$/MgO interface. The position of the $NaNO_3$/MgO interface was determined as the maximum of the derivative of the

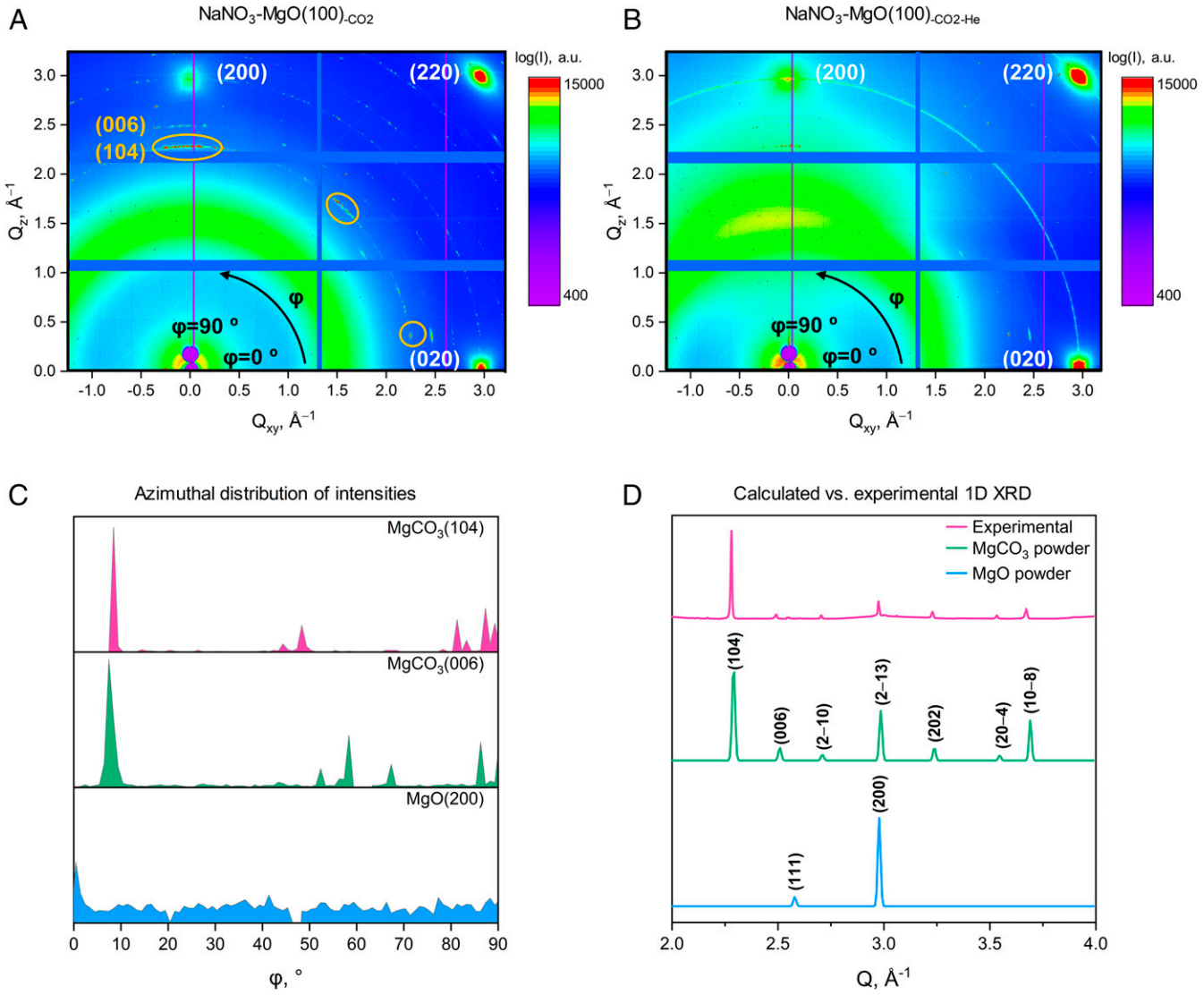

Fig. 2. The 2D GIXRD patterns of (*A*) $NaNO_3$-MgO(100)$_{-CO2}$ and (*B*) $NaNO_3$-MgO(100)$_{-CO2\text{-}He}$. (*C*) Intensity of $MgCO_3$(104) and $MgCO_3$(006) reflections as a function of the azimuthal angle φ in $NaNO_3$-MgO(100)$_{-CO2}$ and the MgO(200) reflection in $NaNO_3$-MgO(100)$_{-CO2\text{-}He}$. (*D*) Azimuthally integrated GIXRD pattern of $NaNO_3$-MgO(100)$_{-CO2}$ (background subtracted) and simulated powder XRD ($Q = 4\pi\cdot\sin(\theta)/\lambda$) patterns of $MgCO_3$ (ICSD: 40117) and MgO (ICSD: 9863).

MgO(220) intensity vs. the sample position (*SI Appendix*, Fig. S13). The fact that the maximum intensity of the $MgCO_3$ reflection is observed close to the position of the $NaNO_3$/MgO interface suggests that $MgCO_3$ grows in the vicinity of the MgO surface, as opposed to a precipitation inside the $NaNO_3$ melt (12, 16). This analysis provided average and microscale information on the location of the formed $MgCO_3$, yet more detailed insight, that is, with higher spatial resolution, into the $MgCO_3$/MgO interface was obtained by HRTEM (*vide infra*).

After carbonation, the sorbent regeneration step, that is, the decomposition of $MgCO_3$ back to MgO, was probed by treating $NaNO_3$-MgO(100)$_{-CO2}$ at 450 °C in He for *ca.* 15 min ($NaNO_3$-MgO(100)$_{-CO2\text{-}He}$). After the regeneration step, the $MgCO_3$ reflections largely disappeared, with only a very weak $MgCO_3$(104) reflection remaining (Fig. 2*B*). We observe the appearance of polycrystalline Debye–Scherrer rings due to MgO, indicating the formation of randomly orientated MgO crystallites after the decomposition of (oriented) $MgCO_3$. This observation is confirmed further by the analysis of the azimuthal distribution of the MgO(200) intensity (Fig. 2*C*). The intensity of MgO is distributed relatively homogeneously, that is, without a clear preferential orientation along φ, indicating a random orientation of the MgO crystallites that are formed via the decomposition of $MgCO_3$ (in Fig. 2*C*, the high-intensity spot of the MgO(100) single crystal substrate is found at *ca.* $\varphi = 0°$).

In summary, in situ XRR shows that, under a CO_2 flow, a surface layer with a lower density and thickness of *ca.* 7 Å forms on bare MgO(100) due to CO_2 sorption; this takes place without appreciable changes in the surface roughness. The surface roughness of MgO changes when coated with $NaNO_3$ (330 °C in He), but even more drastically when exposed to CO_2 (330 °C), due to the formation of highly oriented $MgCO_3$ crystallites at the $NaNO_3$/MgO interface, as opposed to a precipitation with random orientation inside the molten salt (a growth at the TPB cannot, however, be excluded, due to the high mobility of the molten salt). Indeed, the surface roughness of $NaNO_3$-promoted MgO(100) is *ca.* 4 times higher under a CO_2 flow compared to He flow. In the following, we apply electron microscopy (SEM and HRTEM) to provide further insight into 1) the morphology of the $MgCO_3$ crystals formed, 2) MgO surface alterations, and 3) the atomic arrangement at the $MgCO_3$/MgO interface. Since $MgCO_3$ crystals do not form on bare MgO, electron microscopy is only applied to the $NaNO_3$-MgO(100)$_{-CO2}$ system.

Morphology of the $MgCO_3$ Crystals Formed on MgO. To describe the morphology of the $MgCO_3$ product formed during carbonation, we turned to SEM. Pretreatment and carbonation conditions similar to those used in the in situ XRR-GIXRD experiment ($NaNO_3$-MgO(100)-$_{CO2}$) have been used for the as-prepared $NaNO_3$-MgO(100). In addition, a rinsing step in water was necessary to remove the $NaNO_3$ layer and to reveal the $MgCO_3$ product underneath. Prior to morphological analysis, Raman microspectroscopy mapping was used to unequivocally identify the $MgCO_3$ product on the MgO(100) surface (*SI Appendix*, Fig. S6).

The growth habit of the formed magnesium carbonate on $NaNO_3$-$MgO(100)_{CO2\text{-}RW}$ (the subscript RW refers to a rinse in water) as visualized by SEM is shown in Fig. 3 and *SI Appendix*, Fig. S14. Planar views of the $MgCO_3$ are displayed in Fig. 3 *A* and *B*, and a cross-section, obtained by a focused ion beam (FIB) cut, is shown in Fig. 3*C*. SEM demonstrates that, on $NaNO_3$-$MgO(100)_{CO2\text{-}RW}$, $MgCO_3$ grew as individual 2D crystals, or "2D islands," on the surface of MgO with a diameter in the range of 10 μm to 50 μm and a thickness between 0.2 and 2 μm. The observed 2D island-type morphology is in line with in situ GIXRD data which revealed that carbonation of $NaNO_3$-MgO(100) leads to the formation of crystallites of $MgCO_3$ with a marked preferred orientation. The individual $MgCO_3$ islands, exemplified in the images shown in Fig. 3 *A* and *B*, have a growth habit that can be described as a "sectored plate" showing characteristic straight dendrites with triangular tips branching radially from the center of the crystal (45–47). Side branches have grown from the primary branches and coalesced with the $MgCO_3$ product from neighboring branches. At some locations of the surface of $NaNO_3$-$MgO(100)_{CO2\text{-}RW}$, islands of $MgCO_3$ grow separated by up to 200 μm, while, in other locations, the islands have grown closer to each other and merged to form larger clusters as observed in *SI Appendix*, Fig. S15.

Two-dimensional island-type growth with a sectored-plate morphology has been observed previously when precipitating $MgCO_3$ (48), $CaCO_3$ (49), ice crystals (45), and ice analog crystals (Na_2SiF_6) (46) from supersaturated solutions. The growth habits of ice crystals and ice analog crystals have been characterized and mapped in great detail with respect to the level of supersaturation and temperature (46–49). Ice analog crystals such as sodium flourosilicate (Na_2SiF_6) grow in an aqueous solution (crystal growth induced by evaporation), whereby the growth habit depends strongly on the rate of evaporation (i.e., supersaturation level). For lower levels of supersaturation, a compact sectored-plate morphology is obtained, while, for higher levels of supersaturation, a less compact sectored-plate morphology occurs that can turn into stellar dendrites (46). Variations in the growth habit (difference in the length of the primary dendrites compared to the side branches), as observed also in the $MgCO_3$ crystals shown in Fig. 3 *A* and *B*, may thus be a result of local heterogeneities in the level of supersaturation of $MgCO_3$ (i.e., $[Mg^{2+}...CO_3^{2-}]$ ionic pairs). Generally, crystals can form from a supersaturated solution through either homogenous or heterogeneous nucleation (50). Here, the surface of MgO provides heterogeneous nucleation sites (characterized by a lower energy barrier of nucleation in comparison to homogeneous nucleation) (51). It is likely that the $MgCO_3$ nuclei are formed at defect sites on the MgO surface, where it is energetically more favorable for ions to bind (52). Hence, one would expect a polycrystalline powder material containing a variety of exposed facets (yet with the dominant facet being MgO(100)), grain boundaries, and/or defects such as dislocations to have a higher density of potential nucleation sites. Such a nucleation and crystal growth-based mechanism would be described by a sigmoidal-shaped (S-shaped) kinetic curve (50, 53). Indeed, the carbonation of a powder sample of MgO promoted with $NaNO_3$ shows an S-shaped kinetic curve and can be initiated by nuclei seeding (13, 16, 18). The resemblance of nucleation and crystal growth is important because it confirms that the MgO(100) model surface coated with $NaNO_3$ is mechanistically representative for practically more relevant (and scalable) powder samples of MgO promoted with $NaNO_3$.

From the cross-section shown in Fig. 3*C*, it is clear that the carbonate crystal has grown both inward and outward from the original $NaNO_3$/MgO interface (the dashed yellow line represents the location of the nonreacted (i.e., as-received) MgO surface, that is, the $NaNO_3$/MgO interface). A SEM image of the as-received MgO(100) single crystal is shown in *SI Appendix*, Fig. S17. The 2D growth of the carbonate product has a crucial implication for the design of MgO-based sorbents. Considering that $MgCO_3$ appears to grow less than 2 μm in the direction perpendicular to the surface (*z* direction), it will be difficult to fully convert large (thick, >2 μm) MgO crystallites. Hence, this observation suggests that MgO-based CO_2 sorbents

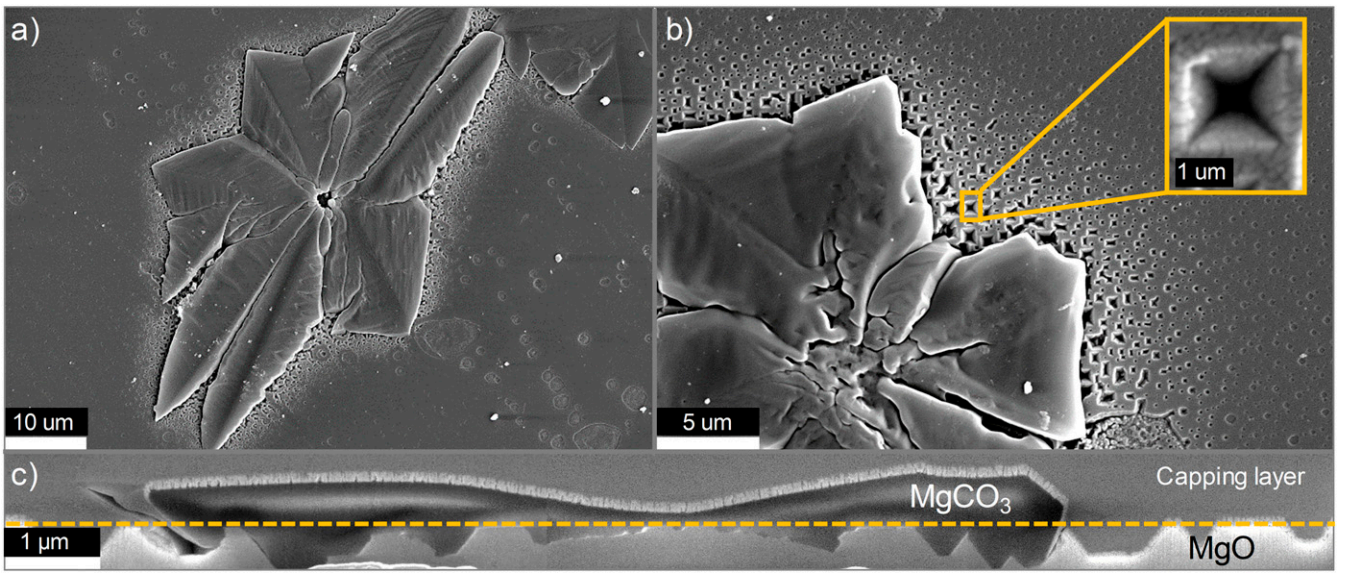

Fig. 3. SEM images of $MgCO_3$ formed on $NaNO_3$-$MgO(100)_{CO2\text{-}RW}$: (*A* and *B*) images of two representative $MgCO_3$ features at different magnifications; *Inset* shows a pyramid-shaped dissolution pit on the MgO surface near the $MgCO_3$ product. (*C*) Cross-section of the $MgCO_3$ product formed on top of MgO. Dashed line highlights the location of the originally flat surface of the MgO(100) single crystal promoted with $NaNO_3$ before its reaction with CO_2.

should have a high MgO surface area that is in contact with $NaNO_3$, which can be achieved by small (i.e., submicrometric) MgO particles/crystallites being coated with alkali metal salt. Further, an excessive growth of the MgO crystallites/particles (over repeated CO_2 capture and regeneration cycles) may, in turn, lead to a deactivation of the sorbents (13, 54).

Etched MgO(100) Surface Surrounding the $MgCO_3$ Product. A very interesting structural feature in Fig. 3 are micrometer-sized pyramidal pits surrounding the magnesium carbonate crystals in $NaNO_3$-MgO(100)-$_{CO2\text{-}RW}$. Firstly, the pits are approximately square-shaped inverse pyramids with the square bases being coorientated and parallel to the [100] direction of MgO(100). Secondly, there is a gradient in the size of the pits, with larger pits (>1 μm) being close to the $MgCO_3$ crystals and a decreasing pit size with increasing distance from the $MgCO_3$ crystal; we do not observe any pits at distances larger than 5 μm to 10 μm away from the $MgCO_3$ crystal. The pits are also present in the MgO substrate below the $MgCO_3$/MgO interface, as can be seen in the cross-section view (Fig. 3*C*). Moreover, a high-angle annular dark-field (ADF) scanning transmission electron microscope (HAADF-STEM) image of the $MgCO_3$/MgO(100) interface reveals a *Z*-contrast (atomic number) gradient in the interface region below the $MgCO_3$ crystal (*SI Appendix*, Fig. S20). The contrast gradient reflects a MgO depletion layer, which is due to the transport of MgO species toward the growing carbonate crystal. Similarly, the gradient of the pyramid size around the carbonate crystal can be considered as a MgO depletion layer along the MgO surface. As the diffusion length of the MgO species toward the $MgCO_3$ crystal increases, the pit sizes decrease. Therefore, the largest etching pits are observed in the vicinity of the carbonate, and there is a gradual decrease in their size with increasing distance from the carbonates. Hence, we can interpret this observation as a 2D hemispherical region of MgO depletion around the $MgCO_3$ product, since it is observed both in the growth plane of the carbonate on the MgO surface and under the 2D carbonate crystals.

Next, we may consider why the depletion of MgO near the surface followed by diffusion would lead to such crystallographically ordered defects (i.e., pyramidal pits). The observed pyramidal shaped pits are analogous to the etching pits observed on single crystalline MgO surfaces that are formed through acid treatment (52, 55, 56). The dissolution of MgO and the etching of pits are initiated preferentially at surface defects (e.g., edge dislocations) and are energetically favored to proceed along the [111] direction of the MgO(100) substrate, forming the characteristic pyramidal shape (52). Moreover, it is well known that diffusion is favored along dislocations, which may accelerate the etching process near the carbonate product (57, 58).

Our samples were rinsed in deionized water (neutral pH) for 1 min to remove the $NaNO_3$ coat, allowing for an SEM analysis of the otherwise buried $MgCO_3$ product. It should be noted that previous studies showed that the formation of the pits required a treatment with an aqueous acid solution (pH = 5.7) for 72 h (52); hence, the pits cannot form during the rinsing step with deionized water. Additionally, a control experiment using $NaNO_3$-coated MgO(100) treated at 420 °C for 1 h and 330 °C for 5 h in N_2 followed by rinsing with deionized water ($NaNO_3$-MgO(100)$_{N2\text{-}RW}$) confirmed the absence of etched pits when the sample was not exposed to a CO_2 flow (*SI Appendix*, Fig. S16). Therefore, based on the similar shape of the etched pyramids in our materials to a material derived via acid etching, we can infer that the observed pits are due to the dissolution of MgO in the presence of both $NaNO_3$ and CO_2 and are presumably initiated at the vicinity of surface defects (52).

Overall, the SEM analysis complements our in situ XRR and GIXRD results providing insight into the 2D growth of $MgCO_3$ islands, and the etching of the MgO surface when both $NaNO_3$ and CO_2 are present (*SI Appendix*, Fig. S16). This suggests that the interaction of CO_2 and $NaNO_3$ leads to a faster rate of MgO dissolution when compared to $NaNO_3$-promoted MgO in an inert gas environment. When the dissolution of MgO (and its reaction with CO_2) yields a critical level of supersaturation, magnesium carbonate will crystallize. Lastly, as soon as $MgCO_3$ is formed, it promotes the further etching of MgO species, which diffuse toward the growing carbonate and provide building blocks for further, increased $MgCO_3$ growth. It is also important to recall that $MgCO_3$ does not nucleate and grow in the absence of a $NaNO_3$ promoter. Therefore, the modification of the MgO(100) surface by molten salts and the enhanced dissolution of MgO under CO_2 likely accelerates the nucleation and growth of $MgCO_3$. In other words, the carbonation reaction is autocatalytic (i.e., the reaction product catalyzes further reaction), and, for such reactions, the product concentration is given by a sigmoidal kinetic behavior as has been observed for powder samples of alkali metal salt-promoted MgO (16). We remark that $NaNO_3$ is mobile on the surface of MgO(100) under the operating conditions, preventing the provision of a definitive answer to the question whether nucleation is most favorable in the TPB (i.e., the portion of the $NaNO_3$/MgO interface in contact with CO_2) or at the "buried" $NaNO_3$/MgO interface. However, the 2D hemispherical shape of the MgO depletion layer around the 2D $MgCO_3$ islands points toward a rapid growth of $MgCO_3$ at the buried $NaNO_3$/MgO interface, as it is unlikely that an expanding TPB exists at the perimeter of a growing 2D $MgCO_3$ crystal. Since both $NaNO_3$ and CO_2 are necessary to facilitate a fast dissolution of MgO, CO_2 must be dissolved (13, 59, 60) in the molten salt to reach the reaction interface.

Atomic Scale Insight into the $MgCO_3$/MgO Interface by TEM. Having established that, under carbonation conditions, 1) a noncrystalline thin (*ca.* 7 Å) surface layer of carbonates forms on bare MgO(100) and 2) MgO(100) coated with $NaNO_3$ leads to the formation of crystallites of $MgCO_3$ with a marked preferred orientation at the interface between $NaNO_3$/MgO, we examine the atomic arrangement at the interface between MgO and the formed $MgCO_3$ crystals by TEM-based techniques.

Spatially resolved electron energy loss spectroscopy (EELS) was utilized to obtain high-resolution information on the electronic structure of the oxygen and carbon atoms, allowing us also to map the phases with high resolution at the interface of $NaNO_3$/MgO(100) in $NaNO_3$-MgO(100)$_{CO2\text{-}RW}$. Similar to the SEM characterization, our TEM analysis focuses on $NaNO_3$-MgO(100)$_{CO2\text{-}RW}$ to gain atomic-scale insight into the formed $MgCO_3$. Fig. 4 shows a HAADF-STEM image of the $MgCO_3$/MgO(100) interface and the simultaneously recorded STEM-EELS data (acquired in the range of 250 eV to 400 eV for C K edge and 520 eV to 620 eV for O K edge). Elemental maps were obtained by background subtraction and the EELS spectrum peak integration using energy windows as shown in Fig. 4 *F* and *G*. From top to bottom, the layers are identified by their electronic structure as amorphous carbon (protection layer of amorphous carbon used for TEM lamella preparation), $MgCO_3$, and MgO. In addition, a clear $MgCO_3$/MgO phase separation is observed, with some overlap between the magnesium carbonate and the oxide phases (marked with arrows on Fig. 4*A*) due to the inclined interface.

To gain insight into the atomic arrangement at the $MgCO_3$/MgO interface, we performed TEM analysis of a FIB cut lamella. Fig. 5*A* shows a selected area electron diffraction (SAED) pattern taken from the cross-section of a TEM lamella that was cut parallel to the (100) plane of the MgO support. Two sets of single crystalline diffraction spots can be observed and one set each assigned to the [100]-zone axis of MgO and the [310]-zone axis of $MgCO_3$. Both diffraction patterns are cooriented along the [001] directions, indicating an epitaxial growth of the $MgCO_3$(001) plane onto the MgO(001) plane. This is in a good agreement with our in situ GIXRD analysis of the sample. More details on the local structure at the interface between MgO and $MgCO_3$ are provided by HRTEM (Fig. 5*B*, viewed along the MgO[100]-zone axis), showing a nearly

CHEMISTRY

coherent interface between the two phases. The diffuse contrast in some regions can be explained by an overlap of the two lattices. An analysis of a further TEM lamella that was cut parallel to the MgO(110) plane provides a further confirmation of the epitaxial growth of $MgCO_3$ onto the MgO support (*SI Appendix*, Fig. S21).

Due to the different crystal structures of the film and the substrate (rhombohedral $MgCO_3$ vs. cubic MgO) and a large lattice mismatch ($MgCO_3$ d_{006} = 2.5 Å; ICSD: 40117; MgO d_{002} = 2.1 Å; ICSD: 9863), one would expect a severely strained $MgCO_3$ film with a compressive strain in the direction perpendicular to the interface. From the HRTEM micrograph in Fig. 5*C*, a strain map is obtained by performing a geometric phase analysis (GPA) (61) along the [001] direction. Indeed, in Fig. 5*D*, compressive strains are observed in the $MgCO_3$ phase at the interface region, but with a strain value below 1% (the regions outside the $MgCO_3$ crystal were not analyzed in the GPA map and correspond to noise). The obtained strain value is considerably lower than the expected value of 15% based on the large lattice mismatch. A possible stress relaxation mechanism in an epitaxial layer that has a large lattice mismatch with a substrate involves the incorporation of misfit dislocations into the interface between the epitaxial layer and substrate (62). Fig. 5*E* shows a bright-field (BF)-STEM image of a cross-section oriented along the MgO [100] direction. In contrast to the interface of the same orientation shown above (Fig. 5*B*, showing the interface viewed along the MgO[100]-zone axis), we can observe the edge-on interface of the $MgCO_3$(006) and the MgO(002) planes in Fig. 5*E*. Fourier filtering of the BF-STEM image using lattice fringes corresponding to the $MgCO_3$(006) and the MgO(002) planes reveals a regular arrangement of misfit dislocations in the $MgCO_3$/MgO interface (Fig. 5*F*). An interface of this type is characteristic for the so-called domain-matching epitaxy, where *m* lattice parameters in the epilayer match with *n* lattice parameters in the substrate. The dimension of the domain is the length of the distance over which lattice matching is achieved repeatedly (63). As the lattice constant of $MgCO_3$ (d_{006} = 2.5 Å) is larger than that of MgO (d_{002} = 2.1 Å), the extra half-planes of the misfit dislocations appear in the MgO substrate. In the region shown, there are two domains of five $MgCO_3$ planes matching six MgO planes, alternating with one domain of six $MgCO_3$ planes matching seven MgO planes (Fig. 5*F*). In addition, due to an inclined interface with respect to the direction of the electron beam, the overlap of the two structures gives rise to a Moiré pattern (see red arrows in Fig. 5*F*). The rotation of the Moiré pattern reflects the angular mismatch between the two lattices.

Collectively, our TEM data reveal an epitaxial growth of the $MgCO_3$ crystal with respect to the MgO substrate in agreement with the preferred orientation observed in our in situ GIXRD analysis. Due to the relatively large mismatch in the lattice constants of $MgCO_3$ and the MgO support, the strained interface is relaxed through the incorporation of lattice misfit dislocations. This type of interface is called domain-matching epitaxy, where *m* lattice parameters in the epilayer match with *n* lattice parameters in the substrate. The domain size is the regularly repeating distance over which lattice matching is maintained.

Conclusions

In conclusion, we have reported on the morphological and structural changes occurring at the surface and interfaces of a model CO_2 sorbent, that is, MgO(100) coated with a $NaNO_3$ promoter under relevant CO_2 capture conditions as obtained by in situ XRR-GIXRD and ex situ SEM and TEM. Our findings provide important puzzle pieces for the elucidation of the role of AMS for the

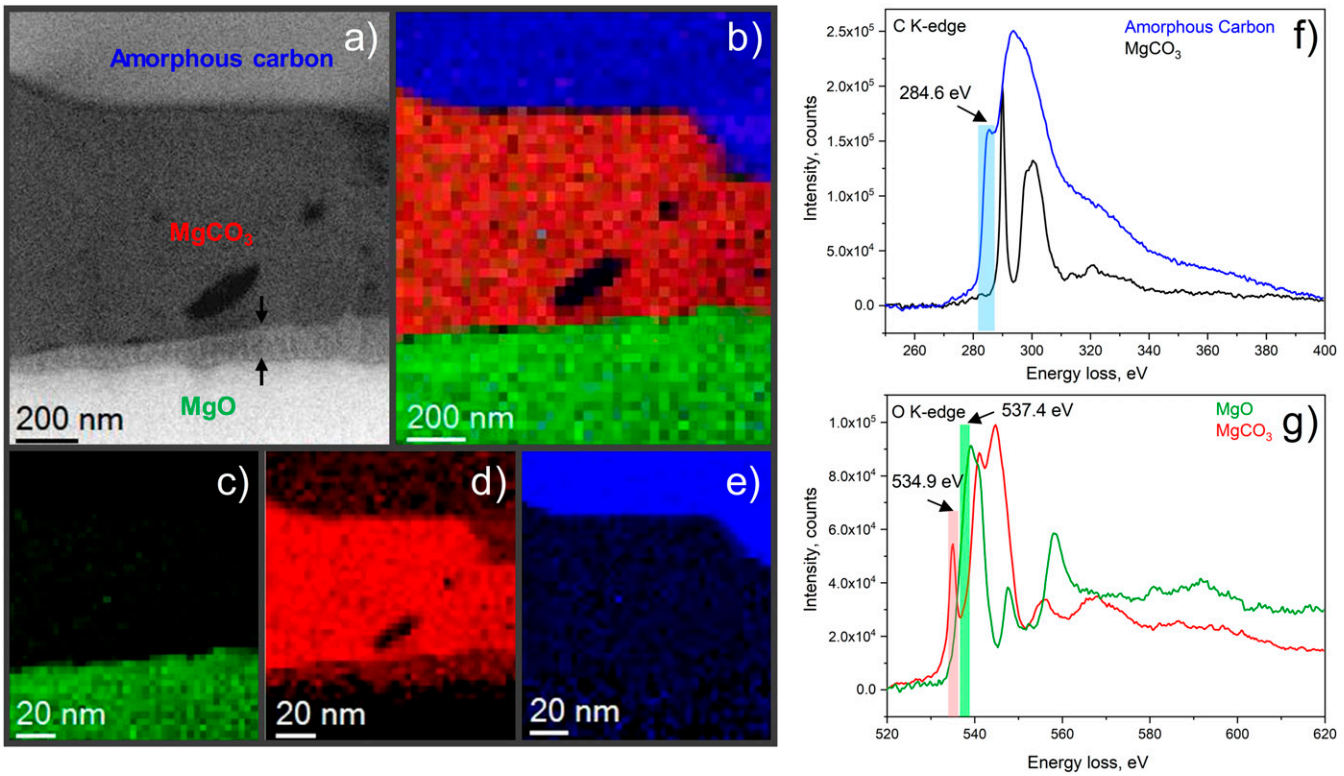

Fig. 4. EELS mapping of the $MgCO_3$/MgO interface oriented along the MgO[100] direction: (*A*) HAADF-STEM image (the arrows show an overlapping region of $MgCO_3$/MgO layers due to the inclined interface); (*B*) overview STEM-EELS elemental maps of the interface. Individual STEM-EELS elemental maps of (*C*) O K edge of MgO, (*D*) O K edge of $MgCO_3$, and (*E*) C K edge of amorphous carbon (protection layer used for TEM lamella preparation); (*F* and *G*) corresponding EELS spectra with marked energy windows used for elemental maps.

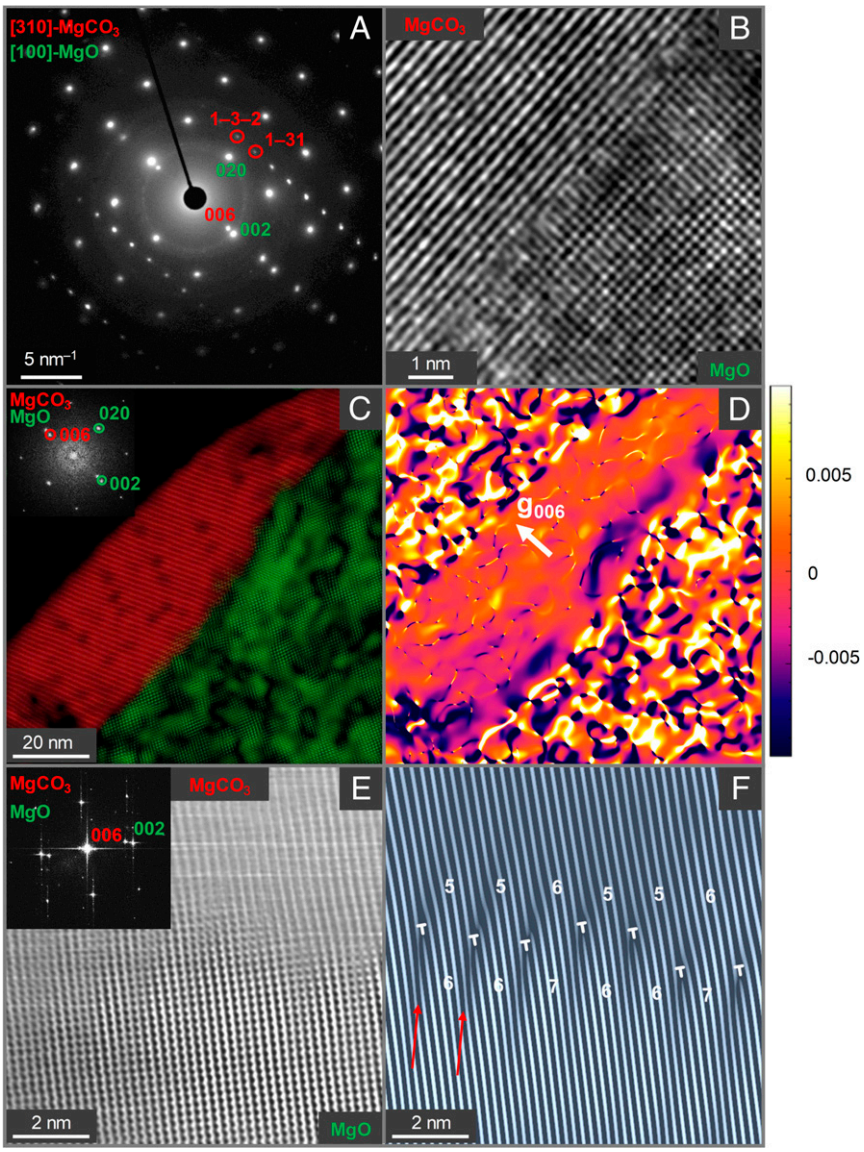

Fig. 5. Structure of the $MgCO_3$/MgO interface and geometrical phase analysis: (*A*) SAED pattern of the TEM lamella oriented along the MgO[100] direction; (*B*) HRTEM micrograph of the interface viewed along the MgO[100] zone axis. (*C*) The inverse FFT pattern obtained by applying a mask to the $MgCO_3$(006) and the MgO(002) reflections in the corresponding fast Fourier transform pattern (*Inset*). (*D*) HRTEM-GPA strain analysis map of the (006) strain component of the $MgCO_3$ film. (*E*) A bright-field STEM image of the edge-on interface viewed along the MgO[100] zone axis (corresponding FFT pattern is shown as an *Inset*); (*F*) inverse Fourier-filtered image showing misfit dislocations in the $MgCO_3$(006) and the MgO(002) plane system; the Moiré patterns are highlighted by red arrows.

rapid CO_2 uptake of MgO. Under practically relevant CO_2 capture conditions, we have observed a roughening of the MgO surface and the formation of $MgCO_3$ crystallites that grow with a preferred orientation on the surface of MgO(100). This work provides in situ evidence that $MgCO_3$ grows favorably at the interface MgO/$NaNO_3$, a finding that will influence the design and rational advancement of more-effective MgO-based CO_2 sorbents. When treated under inert conditions (at 330 °C), the surface roughness of $NaNO_3$-promoted MgO increases by *ca.* 4 Å compared to a pristine MgO(100) crystal, possibly due to MgO dissolution into the melt. The surface roughness increases drastically when the coated sample is also exposed to CO_2. Morphological analyses of the $MgCO_3$ crystals formed by SEM revealed a 2D $MgCO_3$ islands-type growth with a sectored-plate morphology, whereby the thickness of the $MgCO_3$ product is less than 2 μm. The morphology agrees well with a heterogeneous nucleation mechanism followed by crystal growth on the MgO surface. An interesting finding of this work is the observation of pyramidal-shaped micrometer-sized pits that are typically observed after an acidic etching of MgO. The fact that the dissolution of surface MgO into the (molten) $NaNO_3$ promoter is significantly enhanced in a CO_2 atmosphere is presumably due to its acidic nature. HRTEM analysis provides key insight into the atomic arrangement of the $MgCO_3$/MgO interface, revealing an epitaxial growth of a carbonate layer. Due to the lattice mismatch between the magnesium carbonate and the oxide crystals, the carbonate film relaxes through the incorporation of lattice misfit dislocations.

The fundamental knowledge obtained in this work provides guidelines for the design of more-effective MgO-based sorbents by maximizing the AMS/MgO interface area and the density of nucleation sites for the carbonation reaction. This study encourages further research aiming at understanding how to control and enhance the number of nucleation sites at the interface of AMS/MgO

through, for example, seeding and/or defect engineering. An additional aim is to answer the question whether nucleation occurs most favorably at the AMS/MgO interface or the TPB and whether an optimum thickness of the AMS promoter exists to ensure a sufficient coverage for rapid MgO dissolution and to reduce the diffusion length of CO_2 and $[Mg^{2+}...CO_3^{2-}]$ ionic pairs to the reaction interface.

Materials and Methods

In Situ XRR and GIXRD. In situ XRR combined with GIXRD experiments were performed at ID31 of the European Synchrotron Radiation Facility (ESRF). The two materials studied are 1) pristine MgO(100) single crystal and 2) MgO(100) single crystal coated with $NaNO_3$. Both pristine MgO(100) and $NaNO_3$-coated MgO(100) were studied in situ during He treatment and CO_2 uptake conditions. First, the samples were pretreated at 450 °C (10 °C·min^{-1}, 10 mL·min^{-1}) in He for 15 min to reproduce pretreatment conditions that are used typically for the regeneration of $NaNO_3$-promoted MgO sorbents and to allow a comparison with other works in the literature (12, 18, 54) while at the same time preventing the decomposition of $NaNO_3$ (64). Subsequently, the samples were cooled down to 330 °C under He flow and held at this temperature for 15 min. Next, the gas feed was switched to CO_2 (10 mL·min^{-1}) for 90 min, while acquiring XRR followed by GIXRD. Further details about the experimental setup, conditions, and data acquisition scheme can be found in *SI Appendix*, Figs. S2 and S3.

Ex Situ Characterization of the $MgCO_3$ Product on MgO(100) Promoted with $NaNO_3$. Samples for ex situ analysis were prepared in a similar manner as for in situ analysis and tested in a TGA to imitate the conditions during in situ analysis. The as-prepared $NaNO_3$-coated MgO(100) single crystal was pretreated first for 1 h at 420 °C in 80 mL·min^{-1} N_2 to remove surface species. Carbonation was then carried out for 5 h at 330 °C in 80 mL·min^{-1} CO_2 to induce a large degree of carbonation. The heating and cooling rates were 10 °C·min^{-1}. Throughout the program, a purge flow of N_2 25 mL·min^{-1} was used in the TGA.

Raman spectra were collected with a Thermo Scientific Instrument equipped with a 455-nm laser using a spot size of 1.8 μm and 0.6 μm for a magnification of 10× and 100×, respectively. The spectra were acquired in the range of 100 cm^{-1} to 3,500 cm^{-1} with a spectral resolution of 0.96 cm^{-1}.

Cross-sections for SEM were prepared by FIB milling and collected with a Field Electron and Ion (FEI) Scios Dual Beam microscope. TEM lamellas were prepared on the FIB-SEM Helios NanoLab 600i. The FIB cut was parallel to the [100] direction of the single crystalline MgO support.

The microscale and atomic-scale structure of the samples was probed by analytical electron microscopy using a double Cs-corrected (TEM and STEM) JEOL JEM-ARM300F Grand ARM STEM that was operated at 300 kV. The microscope is equipped with the Dual Energy Dispersive Spectroscopy system (two large area silicon drift detectors with 100 mm^2 active area; total solid angle: 1.6 sr) and the Gatan Imaging Filter (GIF) Quantum ER EELS. Before recording the micrographs, the TEM lamella was aligned along the [100]-zone axis of the MgO support. ADF STEM images were recorded with a semi-convergence angle of 18 mrad and 55- to 177-mrad collection semiangles.

Data Availability. All study data are included in the article and *SI Appendix*.

ACKNOWLEDGMENTS. This project has received funding from the European Research Council under the European Union's Horizon 2020 research and innovation program Grant Agreement 819573 and from the Swiss National Science Foundation (Grant 200020_156015). The ESRF is acknowledged for providing access to beam time at ID31 through Proposal MA-3415. We acknowledge the support of ScopeM (ETH) and especially Christian Zaubitzer for his help in TEM lamella preparation. We thank Prof. Dirk Mohr, ETH, for access to FIB-SEM, and Dr. Marianna Diamantpoulou for equipment support. Dr. Maria V. Blanco and Dr. Veijo Honkimäki are kindly acknowledged for providing access to the in situ setup as well as for their support and insightful discussions during the XRR and GIXRD measurements. We acknowledge Fondation Claude et Giuliana and ETH (Grant ETH-44-16-2) for partial financial support.

1. M. Bui *et al.*, Carbon capture and storage (CCS): The way forward. *Energy Environ. Sci.* **11**, 1062–1176 (2018).
2. Y. Hu, Y. Guo, J. Sun, H. Li, W. Liu, Progress in MgO sorbents for cyclic CO_2 capture: A comprehensive review. *J. Mater. Chem. A Mater. Energy Sustain.* **7**, 20103–20120 (2019).
3. H. Sun *et al.*, Progress in the development and application of CaO-based adsorbents for CO_2 capture—A review. *Mater. Today Sustain.* **1–2**, 1–27 (2018).
4. J. Wang *et al.*, Recent advances in solid sorbents for CO_2 capture and new development trends. *Energy Environ. Sci.* **7**, 3478–3518 (2014).
5. M. Bhagiyalakshmi, J. Y. Lee, H. T. Jang, Synthesis of mesoporous magnesium oxide: Its application to CO_2 chemisorption. *Int. J. Greenh. Gas Control* **4**, 51–56 (2010).
6. K. K. Han, Y. Zhou, W. G. Lin, J. H. Zhu, One-pot synthesis of foam-like magnesia and its performance in CO_2 adsorption. *Microporous Mesoporous Mater.* **169**, 112–119 (2013).
7. S. J. Gregg, J. D. Ramsay, Adsorption of carbon dioxide by magnesia studied by use of infrared and isotherm measurements. *J. Chem. Soc. A Inorg. Phys. Ther.* **1**, 2784–2787 (1970).
8. S. Choi, J. H. Drese, C. W. Jones, Adsorbent materials for carbon dioxide capture from large anthropogenic point sources. *ChemSusChem* **2**, 796–854 (2009).
9. A. M. Ruminski, K. J. Jeon, J. J. Urban, Size-dependent CO_2 capture in chemically synthesized magnesium oxide nanocrystals. *J. Mater. Chem.* **21**, 11486–11491 (2011).
10. K. Zhang *et al.*, Roles of double salt formation and $NaNO_3$ in Na_2CO_3-promoted MgO absorbent for intermediate temperature CO_2 removal. *Int. J. Greenh. Gas Control* **12**, 351–358 (2013).
11. A. T. Vu, Y. Park, P. R. Jeon, C. H. Lee, Mesoporous MgO sorbent promoted with KNO_3 for CO_2 capture at intermediate temperatures. *Chem. Eng. J.* **258**, 254–264 (2014).
12. K. Zhang *et al.*, Phase transfer-catalyzed fast CO_2 absorption by MgO-based absorbents with high cycling capacity. *Adv. Mater. Interfaces* **1**, 1400030 (2014).
13. T. Harada, F. Simeon, E. Z. Hamad, T. A. Hatton, Alkali metal nitrate-promoted high-capacity MgO adsorbents for regenerable CO_2 capture at moderate temperatures. *Chem. Mater.* **27**, 1943–1949 (2015).
14. X. Zhao *et al.*, Mesoporous MgO promoted with $NaNO_3$/$NaNO_2$ for rapid and high-capacity CO_2 capture at moderate temperatures. *Chem. Eng. J.* **332**, 216–226 (2018).
15. H. Cui *et al.*, Ultrafast and stable CO_2 capture using alkali metal salt-promoted MgO-$CaCO_3$ sorbents. *ACS Appl. Mater. Interfaces* **10**, 20611–20620 (2018).
16. S. I. Jo *et al.*, Mechanisms of absorption and desorption of CO_2 by molten $NaNO_3$-promoted MgO. *Phys. Chem. Chem. Phys.* **19**, 6224–6232 (2017).
17. J. Ding *et al.*, Enhanced CO_2 adsorption of MgO with alkali metal nitrates and carbonates. *Appl. Energy* **263**, 114681 (2020).
18. A. Dal Pozzo, A. Armutlulu, M. Rekhtina, P. M. Abdala, C. R. Müller, CO_2 uptake and cyclic stability of MgO-based CO_2 sorbents promoted with alkali metal nitrates and their eutectic mixtures. *ACS Appl. Energy Mater.* **2**, 1295–1307 (2019).
19. C. H. Lee *et al.*, Na_2CO_3-doped CaO-based high-temperature CO_2 sorbent and its sorption kinetics. *Chem. Eng. J.* **352**, 103–109 (2018).
20. M. Rekhtina *et al.*, Effect of molten sodium nitrate on the decomposition pathways of hydrated magnesium hydroxycarbonate to magnesium oxide probed by in situ total scattering. *Nanoscale* **12**, 16462–16473 (2020).
21. G. A. Mutch *et al.*, Carbon capture by metal oxides: Unleashing the potential of the (111) facet. *J. Am. Chem. Soc.* **140**, 4736–4742 (2018).
22. S. J. Park, Y. Kim, C. W. Jones, $NaNO_3$-promoted mesoporous MgO for high-capacity CO_2 capture from simulated flue gas with isothermal regeneration. *ChemSusChem* **13**, 2988–2995 (2020).
23. R. N. Kust, J. D. Burke, Thermal decomposition in alkali metal nitrate melts. *Inorg. Nucl. Chem. Lett.* **6**, 333–335 (1970).
24. H. Jeon *et al.*, Unveiling the carbonation mechanism in molten salt-promoted MgO-Al_2O_3 sorbents. *J. CO2 Util.* **39**, 101153 (2020).
25. H. Lee *et al.*, In situ observation of carbon dioxide capture on pseudo-liquid eutectic mixture-promoted magnesium oxide. *ACS Appl. Mater. Interfaces* **10**, 2414–2422 (2018).
26. A. Sasahara, T. Murakami, M. Tomitori, Hydration of MgO(100) surface promoted at <011> steps. *J. Phys. Chem. C* **119**, 8250–8257 (2015).
27. M. D. Susman, H. N. Pham, A. K. Datye, S. Chinta, J. D. Rimer, Factors governing MgO(111) faceting in the thermal decomposition of oxide precursors. *Chem. Mater.* **30**, 2641–2650 (2018).
28. G. Renaud, R. Lazzari, F. Leroy, Probing surface and interface morphology with grazing incidence small angle X-ray scattering. *Surf. Sci. Rep.* **64**, 255–380 (2009).
29. C. Chizallet, G. Costentin, M. Che, F. Delbecq, P. Sautet, Infrared characterization of hydroxyl groups on MgO: A periodic and cluster density functional theory study. *J. Am. Chem. Soc.* **129**, 6442–6452 (2007).
30. D. Cornu, H. Guesmi, J. M. Krafft, H. Lauron-Pernot, Lewis acido-basic interactions between CO_2 and MgO surface: DFT and DRIFT approaches. *J. Phys. Chem. C* **116**, 6645–6654 (2012).
31. P. Liu, P. M. Abdala, G. Goubert, M.-G. Willinger, C. Copéret, Ultrathin single crystalline MgO(111) nanosheets. *Angew. Chem. Int. Ed. Engl.* **60**, 3254–3260 (2021).
32. M. Mezger *et al.*, High-resolution in situ x-ray study of the hydrophobic gap at the water–octadecyl-trichlorosilane interface. *Proc. Natl. Acad. Sci. U.S.A.* **103**, 18401–18404 (2006).
33. M. Yasaka, X-ray thin-film measurement techniques. *Rigaku J.* **26**, 1–9 (2010).
34. P. A. Fenter, X-ray reflectivity as a probe of mineral-fluid interfaces: A user guide. *Rev. Mineral. Geochem.* **49**, 149–221 (2002).
35. D. K. Aswal *et al.*, XPS and AFM investigations of annealing induced surface modifications of MgO single crystals. *J. Cryst. Growth* **236**, 661–666 (2002).
36. J. Jupille, G. Thornton, *Defects at Oxide Surfaces* (Springer, 2015).
37. G. Pacchioni, H. Freund, Electron transfer at oxide surfaces. The MgO paradigm: From defects to ultrathin films. *Chem. Rev.* **113**, 4035–4072 (2013).
38. F. Rieutord, R. Simon, B. Beau, X-ray synchrotron radiation study of rare-gas film growth. *Physica B* **221**, 215–217 (1996).

39. F. Rieutord, R. Simon, R. Conradt, P. Müller-Buschbaum, Surface melting and preroughening of argon: An X-ray reflection study. *EPL (Europhysics Lett.)* **37**, 565 (1997).
40. C. Chizallet *et al.*, Assignment of photoluminescence spectra of MgO powders: TD-DFT cluster calculations combined to experiments. Part I: structure effects on dehydroxylated surfaces. *J. Phys. Chem. C* **112**, 16629–16637 (2008).
41. I. K. Robinson, Crystal truncation rods and surface roughness. *Phys. Rev. B Condens. Matter* **33**, 3830–3836 (1986).
42. M. B. Jensen, L. G. M. Pettersson, O. Swang, U. Olsbye, CO_2 sorption on MgO and CaO surfaces: A comparative quantum chemical cluster study. *J. Phys. Chem. B* **109**, 16774–16781 (2005).
43. J. Schlipf, P. Müller-Buschbaum, Structure of organometal halide perovskite films as determined with grazing-incidence X-ray scattering methods. *Adv. Energy Mater.* **7**, 1700131 (2017).
44. J. Ogle, D. Powell, E. Amerling, D.-M. Smilgies, L. Whittaker-Brooks, Quantifying multiple crystallite orientations and crystal heterogeneities in complex thin film materials. *CrystEngComm* **21**, 5707–5720 (2019).
45. M. P. Bailey, J. Hallett, A comprehensive habit diagram for atmospheric ice crystals: Confirmation from the laboratory, AIRS II, and other field studies. *J. Atmos. Sci.* **66**, 2888–2899 (2009).
46. M. J. Krasiński, J. Prywer, Growth morphology of sodium fluorosilicate crystals and its analysis in base of relative growth rates. *J. Cryst. Growth* **303**, 105–109 (2007).
47. X. Zhai, W. Wang, G. Zhang, B. He, Crystal pattern formation and transitions of PEO monolayers on solid substrates from nonequilibrium to near equilibrium. *Macromolecules* **39**, 324–329 (2006).
48. B. Sun *et al.*, Preparation of basic magnesium carbonate by simultaneous absorption of NH_3 and CO_2 into $MgCl_2$ solution in an RPB. *Powder Technol.* **284**, 57–62 (2015).
49. N. Andritsos, A. J. Karabelas, P. G. Koutsoukos, Morphology and structure of $CaCO_3$ scale layers formed under isothermal flow conditions. *Langmuir* **13**, 2873–2879 (1997).
50. N. T. K. Thanh, N. Maclean, S. Mahiddine, Mechanisms of nucleation and growth of nanoparticles in solution. *Chem. Rev.* **114**, 7610–7630 (2014).
51. D. E. Bugaris, H. C. zur Loye, Materials discovery by flux crystal growth: Quaternary and higher order oxides. *Angew. Chem. Int. Ed. Engl.* **51**, 3780–3811 (2012).
52. J. A. Mejias, A. J. Berry, K. Refson, D. G. Fraser, The kinetics and mechanism of MgO dissolution. *Chem. Phys. Lett.* **314**, 558–563 (1999).
53. M. Suemitsu, H. Togashi, T. Abe, Autocatalytic reaction model: A phenomenology for nucleation-coalescence-growth of thin films. *Thin Solid Films* **428**, 83–86 (2003).
54. A. T. Vu, K. Ho, S. Jin, C. H. Lee, Double sodium salt-promoted mesoporous MgO sorbent with high CO_2 sorption capacity at intermediate temperatures under dry and wet conditions. *Chem. Eng. J.* **291**, 161–173 (2016).
55. K. Sangwal, Mechanism of dissolution of MgO crystals in acids. *J. Mater. Sci.* **15**, 237–246 (1980).
56. K. Sangwal, T. C. Patel, Etching studies on {100} faces of MgO crystals in H_3PO_4 acids. *Krist. Tech.* **13**, 281–287 (1978).
57. W. J. Bowman, A. Darbal, P. A. Crozier, Linking macroscopic and nanoscopic ionic conductivity: A semiempirical framework for characterizing grain boundary conductivity in polycrystalline ceramics. *ACS Appl. Mater. Interfaces* **12**, 507–517 (2020).
58. J. M. Polfus, B. Yildiz, H. L. Tuller, Origin of fast oxide ion diffusion along grain boundaries in Sr-doped $LaMnO_3$. *Phys. Chem. Chem. Phys.* **20** 19142–19150 (2018).
59. E. Sada, S. Katoh, H. Yoshii, I. Takemoto, N. Shiomi, Solubility of carbon dioxide in molten alkali halides and nitrates and their binary mixtures. *J. Chem. Eng. Data* **26**, 279–281 (1981).
60. T. Harada, T. A. Hatton, Colloidal nanoclusters of MgO coated with alkali metal nitrates/nitrites for rapid, high capacity CO_2 capture at moderate temperature. *Chem. Mater.* **27**, 8153–8161 (2015).
61. M. J. Hÿtch, E. Snoeck, R. Kilaas, Quantitative measurement of displacement and strain fields from HREM micrographs. *Ultramicroscopy* **74**, 131–146 (1998).
62. M. A. Herman, W. Richter, H. Sitter, *Epitaxy: Physical Principles and Technical Implementation* (Springer Series in Materials Science, Springer Science & Business Media, 2004), vol. 62.
63. T. Zheleva, K. Jagannadham, J. Narayan, Epitaxial growth in large-lattice-mismatch systems. *J. Appl. Phys.* **75**, 860–871 (1994).
64. Y. Qiao *et al.*, Alkali nitrates molten salt modified commercial MgO for intermediate-temperature CO_2 capture: Optimization of the Li/Na/K ratio. *Ind. Eng. Chem. Res.* **56**, 1509–1517 (2017).
65. B. K. Tanner, "Grazing incidence X-ray reflectivity and scattering" in *Handbook of Advanced Non-Destructive Evaluation*, N. Ida, N. Meyendorf, Eds. (Springer International, 2018), pp. 1–34.